ABSTRACT

Economic production from extremely low matrix permeability unconventional reservoirs is usually accomplished through multi-stage slickwater hydraulic fracturing which generates opening mode hydraulic fractures and induces shear slip on pre-existing fractures in the surrounding formation. Production decline curves during the early years of production from thousands of wells in four unconventional plays in the U.S. (two oil, two gas) indicate that 1) production is dominated by linear flow from the matrix into much more permeable fracture planes, 2) the rapid decrease in production rates is a natural consequence of depletion in these extremely low permeability formations and 3) the cumulative area of permeable fracture planes created during stimulation is a key factor influencing ultimate resource recovery. The role of stimulated slip on pre-existing fractures and faults on production is estimated by modeling the area of the fracture network implied by microseismicity associated with hydraulic fracturing operations using two case studies in the Barnett Shale. We assess the total fracture area created during stimulation on a stage-by-stage basis and compare this with relative stage-by-stage production data from distributed temperature sensing.

INTRODUCTION

Hydrocarbon production from unconventional reservoirs relies on diffusion from low permeability matrix to high permeability fracture networks. Typical matrix permeabilities in major unconventional resource reservoirs are in the nanodarcy to microdarcy ranges (Luffel, Hopkins, and Schettler, 1993; Heller, Vermylen, and Zoback, 2014; Bhandari et al., 2015; Al-Ismail and Zoback, 2016). Multi-stage hydraulic fracturing enhances production from these extremely low permeability reservoirs by inducing opening mode hydraulic fractures that extend

from horizontal wells in a direction perpendicular to the minimum horizontal principal stress. Importantly, using low viscosity slickwater as a fracturing fluid, leak-off of pressure from the hydraulic fracture planes increases pore pressure in the surrounding rock mass, triggering shear slip on pre-existing fractures and faults. Shear deformation on rugose planes increases permeability through dilatancy, even with slip magnitudes of less than 0.1 mm (Ye et al., 2017).

Figure 1 shows average decline curves for thousands of unconventional oil (Eagleford, Bakken) and gas (Barnett, Marcellus) wells. Wells with less than 24 months of reported active production are excluded. The wells are grouped into two year cohorts starting with the first production date. Mean monthly production is calculated as a function of months active. Cohorts with less than 350 wells are excluded. After filtering out wells that do not meet data quality requirements, 45,440 wells remain, with more than 7,500 wells in each reservoir.

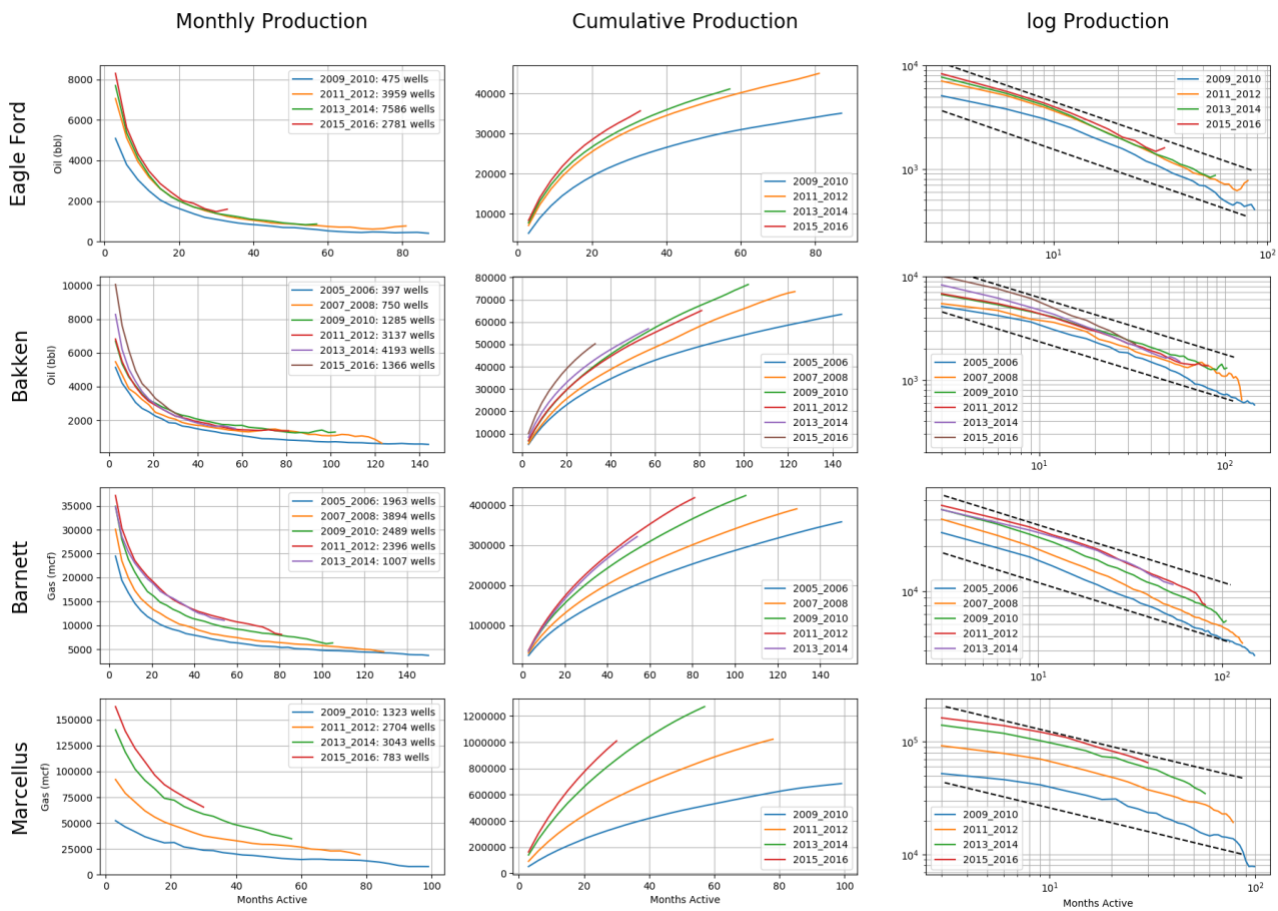

Figure 1: Production is grouped and averaged by reservoir in two year increments. The left column shows monthly production rates, the center column shows cumulative production and the right column shows monthly production rates in log-log space to demonstrate that production rated decline with a rate similar to time-1/2 (as indicated by the dashed lines).

As is well known, production rates decrease rapidly during the first years of production (left column in Figure 1). While individual wells show complex behavior due to operational issues and frequent interventions targeted at improving production, averaging across many wells provides reasonably clean decline curves. Note that in each reservoir, improved production practices result in initial production rates that increase monotonically from each two year cohort to the next. This is most dramatic in the Barnett and Marcellus. The center column shows cumulative production as a function of time. Mirroring the production rate data, an increase in cumulative production is seen from one cohort to another. It is heartening that the most recently drilled wells in the Eagle Ford, Bakken and Marcellus show significant increases in cumulative

production, even after 3 years of production. The right column shows monthly production rates in log-log space to demonstrate that production rates decline with a rate similar to time$^{-1/2}$, as indicated by the dashed lines.

To first order, the data shown in Figure 1 indicate linear flow from extremely low matrix permeability to much more permeable planes. In linear flow, production rate is proportional to time$^{-1/2}$ as given by

$$q = \frac{1}{2}\frac{\alpha}{\sqrt{t}} \tag{1}$$

For dry gas reservoirs,

$$\alpha = A\left(\frac{P_r^2 - P_{bhf}^2}{P_s}\right)\sqrt{\frac{c_g \phi_m k_m}{\pi \eta}} \tag{2}$$

where A is the total surface area of all fractures (the hydraulic fractures and shear fractures) in contact with the matix, P_r is the reservoir pressure, P_{bhf} is the bottom hole flowing pressure, P_s is atmospheric pressure, c_g is gas compressibility, ϕ_m is matrix porosity, η is the gas viscosity, and k_m is matrix permeability. For oil, c_g is replaced by a constant with units pressure^{-1} and the driving pressure term is slightly different (Katz, 1959). Cumulative production is obtaining by integrating (1) is thus given by

$$Q = \alpha\sqrt{t} \tag{3}$$

which is shown in the center column of Figure 1.

To emphasize the observation that production rate declines with time$^{-1/2}$, we re-plotted the data in the left column of Figure 1 in the right column in log-log space. This implies that $\log(q)$ should decline with a slope of ½ as indicated by

$$\log(q) = \log\left(\frac{1}{2}\alpha\right) - \frac{1}{2}\log(t) \quad (4)$$

During the first three years of production, the average slope for all two-year increments for all reservoirs shown in Figure 1 is -0.503, with an R^2 value of 0.98, indicating linear flow during the first several years of production. With data from only 66 wells, Patzek et al. (2014) also noted average production rates decreasing as time$^{-1/2}$ in the Barnett shale. As indicated in Eqn. 2, If one considers stimulation of any given well (or perhaps an average well for each of these reservoirs) cumulative production is going to depend on the total surface area in contact with the reservoir. Maximizing permeable area during stimulation, therefore is needed to maximize production. Note in the right hand column of Figure 1 that as production continues, the slope steepens slightly with an average slope of -0.54 for the first 5 years. This might reflect matrix permeability (or fracture conductivity) decreasing with depletion or a slow transition to radial flow which would imply a slope of -1.

MICROSEISMICITY TO FRACTURE NETWORKS IN THE BARNETT

While not all shear slip on pre-existing faults stimulated during hydraulic fracturing results in detectable seismicity (see Zoback et al., 2012; Kohli and Zoback, 2013), microseismic event locations and focal mechanisms analysis can be used to provide meaningful insight into the stimulated fracture network. Shear fracture networks, specifically pre-existing planar discontinuities such as fractures and faults that have slipped due to increased pore pressure

during hydraulic fracturing, are characterized by fracture intensity, orientation, size, and spatial distribution. In the sections below, we argue that these parameters impact production from unconventional reservoirs because they control the distance that hydrocarbons must flow through the matrix to reach a high permeability pathway to the hydrofrac and then to the wellbore. Given the extremely low matrix permeability of unconventional reservoirs, introducing as much surface area as possible during stimulation effectively minimizes diffusion distances through the matrix, thus enhancing production through stimulation.

In the next sections, we analyze two microseismic data sets gathered during hydraulic fracturing operations in the Barnett shale, which will be referred to as Barnett I and II. In both data sets, each fracture stage was monitored by two downhole geophone arrays. Figure 2 shows plan views of the stimulated wells, the wells in which microseismic monitoring arrays were deployed, and associated microseismicity. Microseismic event intensity varies significantly by stage, and event locations sometimes scatter across multiple stages. This can result from 1) inaccurate event locations (Hakso and Zoback, 2017 discuss the uncertainties in the locations of the Barnett I data set), 2) microseismic events propagating along pre-existing fault systems, as seems to be the case for several stages in the Barnett II data set (Farghal and Zoback, 2015), or poor zonal isolation, as is especially clear for stage 2 (green dots) in the Barnett II data set. Note that many stage 2 events occur in the vicinity of stage 1.

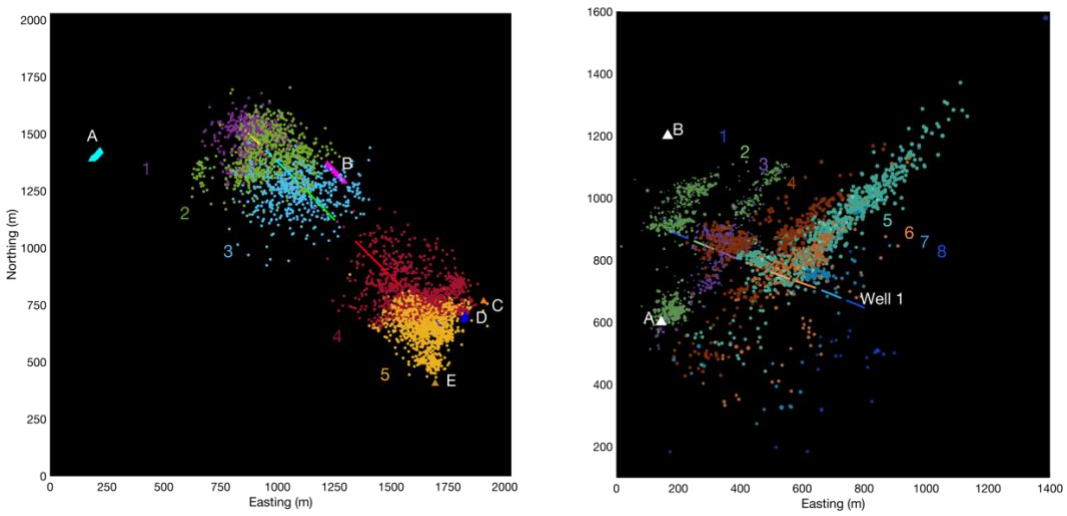

Figure 2: Plan view of two hydraulically stimulated wells in the Barnett with associated seismicity: Barnett I (left) and Barnett II (right). In the Barnett I data set, seismic monitoring arrays were deployed in two of the 5 wells labeled A-E. In the Barnett II data set, monitoring of all 8 stages was done from monitoring wells A and B. The individual stages (and associated microseismicity) is indicated by numbers and colors.

Figure 3 is a heuristic illustration of the manner in which elevated pore pressure during hydraulic fracturing triggers slip in Barnett I using Mohr circles and stereonets. The state of stress was determined for this data set using established methods (Kuang et al., 2017). A normal/strike-slip faulting stress state is appropriate for this area, noting that the vertical stress (S_V) is the maximum principal stress but the maximum horizontal principal stress (S_{Hmax}) is only slightly less. Note that in the Mohr circles shown, the abscissa indicates total stress, S_{ij}, not effective stress. Presentation in this manner makes the intercept of the friction faulting line correspond to the initial pore pressure. For the purposes of illustration, we assume near hydrostatic pore pressure and a coefficient of friction of 0.6. We ignore cohesion, which is likely quite small. The Barnett is only slightly overpressured and friction can vary depending on clay content, but an average value of about 0.6 is quite reasonable (Kohli and Zoback, 2013). The fracture planes shown in the Mohr circle and stereonet images in the upper part of Figure 3a were obtained from an image log in the horizontal well. The planes in the lower part of Figure 3a

represent the slip planes determined from the focal plane mechanisms and knowledge of the stress state (Kuang et al., 2017). For comparison, the total number of planes shown was scaled to show a comparable number, as shown in the upper part of the figure, as focal plane mechanisms could be computed only for the 113 largest events. In blue and yellow we also show hypothetical planes normal to S_{hmin} (sub-parallel to hydraulic fractures) and normal to S_{Hmax}, respectively, because it is sometimes assumed that pre-existing fractures in unconventional reservoirs are aligned parallel and perpendicular to the current principal stresses. We also show in green a hypothetical plane normal to S_V (simulating horizontal bedding planes) as it is often argued that bedding plane slip is significant during hydraulic fracturing.

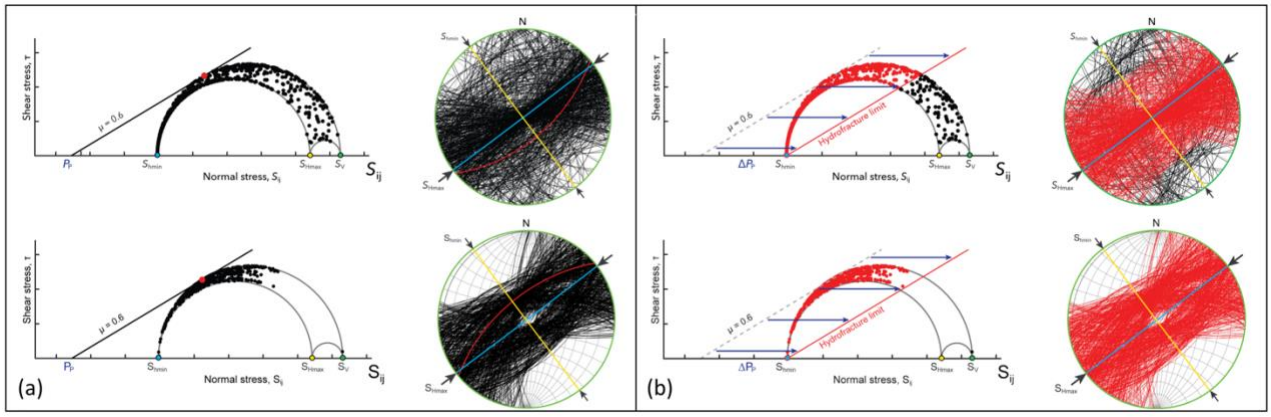

Figure 3: Mohr diagrams and stereonets illustrating the shear and normal stress on pre-existing fractures observed in the wellbore image log (upper figures) and planes obtained from focal mechanisms where the likely slip plane was identified (lower figures). a) The unstimulated case. Almost none of the fractures are expected to slip in the current stress field. b) The stimulated case. The planes shown in red are expected to slip if the pore pressure on the plane reaches the value of the least principal stress (the frac gradient).

The Mohr diagrams in Figure 3a represents the reference state prior to stimulation. Almost no fractures/faults are well-oriented for slip in the current field. In other words, the great majority of planes are inactive fractures and faults, often mineralized with calcite (Gale et al., 2014). Figure 3b shows in red the fractures which slip when pore pressure is raised to the magnitude of the least principal horizontal stress (the fracture gradient) due to pressure leak-off

during hydraulic fracturing. As shown, when the pressure reaches the frac gradient the majority of planes are expected to slip. The planes that do not slip are roughly perpendicular S_{Hmax} (striking NW-SE with steep dip) or sub-horizontal. For the purposes of illustration, we neglected *net pressure*, the amount that the pressure during hydraulic fracturing exceeds the least principal stress due viscous resistance during pumping. This is typically on the order of a several MPa (a few hundred psi) and falls off quickly away from hydraulic fracture near the wellbore. Note also the similarity between the distribution of the faults which slip in response to elevated pore pressure in both the fault planes observed in the image log and those inverted from the focal mechanism analysis. The planes shown in Figure 3b represent planes that did slip and produce microseismic events. Thus, the excellent comparison between these figures provides support for the fact that much of the pressure acting in the hydraulic fractures during stimulation is reaching each of the fault planes to initiate slip, thereby indicating creation of an interconnected, permeable fracture network in contact with the relatively impermeable shale matrix.

The area, S, associated with each event is calculated through the seismic moment, M_o, and stress drop, $\Delta\tau$. For a circular fault, area is given as (Stein and Wysession, 2003):

$$S = \pi \left(\frac{7M_o}{16\Delta\tau} \right)^{\frac{2}{3}} \quad (5)$$

Note that, somewhat unintuitively, stress drop and fault patch size are inversely related. Calculating stress drops for microseismic data is extremely difficult due to the limited bandwidth of the recorded seismograms. Because of the extremely small size of microseismic events, data to several thousand Hz would be needed. From other studies, we know that stress drop distributions are scale invariant and generally follow a log-normal distribution (Allmann and Shearer, 2009; Imanishi and Ellsworth, 2006). A number of studies (e.g. Goertz-Allmann,

Goertz, and Wiemer, 2011; Clerc et al., 2016; Huang, Beroza, and Ellsworth, 2016; Cocco, Tinti, and Cirella, 2016) have examined stress drops over an extremely wide range of earthquake sizes. Each study finds values in the range from 10^{-1} to 10^{2} MPa, with single digit median stress drops and no discernible trend with earthquake size. Complete stress drop for a given geomechanical context provides an upper bound (the maximum available shear stress in the studies reported here is ~8.5 MPa). In this study, a log-normal stress drop distribution is constructed such that few events exceed complete stress drop, and the standard deviation is representative of empirical studies of average stress drops found in the literature. Hence, the distribution is centered on a stress drop of 0.5 MPa. Note that the radius is proportional to the cube root of the stress drop, mitigating the impact of any difference between assumed and actual stress drop distributions.

To visualize the fracture networks implied by the microseismicity, Figure 4 shows a 100x100x100m visualization in the area of the densest concentration of seismicity in the vicinity of stage 4 of the Barnett I data set. Fracture locations and orientations are assigned from microseismic event distributions and focal mechanism inversion respectively. Note that there is a wide distribution of shear fractures and fracture orientations in the area between the hydraulic fractures, implying a well-connected network of shear fractures in contact with the low permeability matrix. Unfortunately, it is not feasible to consider this image a realistic representation of the fracture network given the large relative location uncertainties in this data set (Hakso and Zoback, 2017). Because of this, and because the total production is controlled by the total area of permeable fractures in contact with the reservoir (Eqns. 1, 2) the fracture networks modeled in this study should be viewed as statistically representative, rather than as precise models.

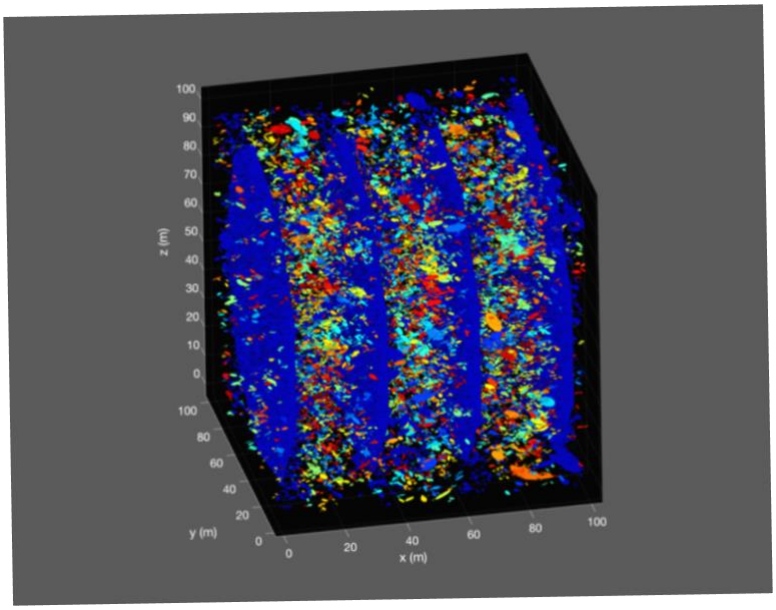

Figure 4: Visualization of the area of the densest concentration of seismicity in the vicinity of stage 4 of the Barnett I data set. Fracture locations and orientations are assigned from microseismic event distributions and focal mechanism inversion respectively. Note that there is a wide distribution of shear fractures and fracture orientations in the area between the hydraulic fractures, implying a well-connected network of shear fractures.

To consider the total stimulated area in each stage and compare it to relative production, the Barnett II data set will be used. Although there are no focal mechanisms available for this data set, there is a distributed temperature sensing fiber that was used to estimate relative gas production from each stage (Roy et al., 2014). The magnitude distribution for the events in Barnett II are shown in Figure 5a. Note the very high "b" slope, characteristic of microseismic data sets (e.g., Maxwell, 2014). Randomly drawing from the empirical stress drop distribution yields a median source radius of approximately one meter as most events are approximately magnitude -2 (Figure 5b). Figure 5c shows plan views of fracture networks generated from stress drop distributions with median stress drops of 0.5 and 0.1 MPa to illustrate the impact of a 5 fold change in the median stress drop. To calculate total surface area from the microseismicity created in every stage, we extrapolated the total number of events down to magnitude -2.25.

Although many more smaller events might have occurred, we did not extrapolate the number of events further because we did not want to extrapolate too far from the observations and smaller magnitudes are associated with very small amounts of slip and surface area. Similarly, aseismic slip may be occurring during stimulation (Zoback et al., 2012). Thus, the area we calculate from the microseismic events represents a lower bound of the created surface area. In the discussion below, we will focus on the relative area created from stage to stage.

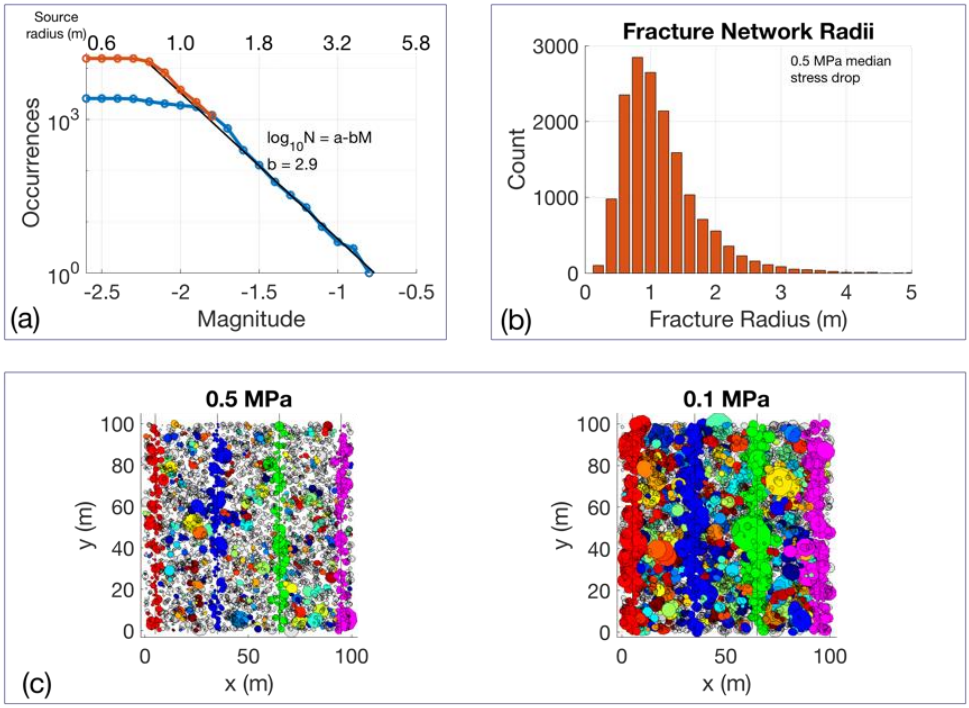

Figure 5: (a) The earthquake catalog is complete to approximately -1.9, here extrapolated to -2.25. (b) this results in a distribution of fracture radii with a median fracture radius of 1.08 meters, with a long tail to the right. (c) Assuming a 5x smaller stress drop in a representative region of dense seismicity results in a fracture network with 40% smaller fracture radii, but otherwise identical characteristics.

EVOLUTION OF FRACTURE AREA AND IMPLICATIONS FOR PRODUCTION

The eight histograms in Figure 6 display the observed number of microearthquakes (extrapolated down to M -2.25) associated with each of the 8 hydraulic fracturing stages in Barnett II as well as the cumulative area created, calculated in the manner described above. The left side of the figure shows the relative stage-by-stage production data calculated from DTS data obtained at two different times during production (Roy et al., 2014). The total size of the stimulated fracture network associated with each stage varies dramatically, ranging from less than 100 m^2 in stages 1 and 8 to nearly 30,000 m^2 in stage 5. The total surface area created in all the stages was at least 76,000 m^2.

It is clear that the stages with most production (4, 5 and 6) are also the stages in which the most surface area was created. While very little surface area was created by shearing in several stages, there is still a small amount of production, perhaps associated with the area of the hydraulic fractures themselves, or aseismic slip. The duration of injection required to achieve a significant amount of permeable area varies from stage to stage. In stage 2, the limited amount of surface area created occurred after 140 minutes of pumping, whereas almost none occurred after that amount of time in stage 4. It should be noted that area is assigned to a specific stage if the microseismic event occurred during that stage, independent of the location of the event. It was pretty clear after a relatively short pumping time that stages 1, 7 and 8 were unlikely to produce much area.

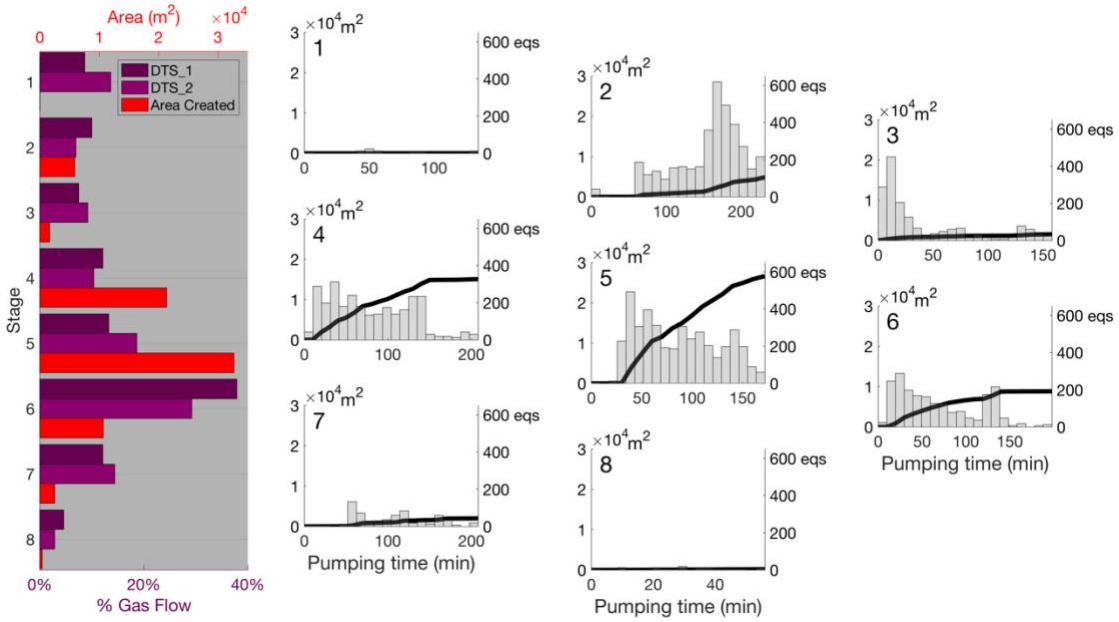

Figure 6: Production, as measured by distributed temperature sensing, correlated with area created per stage (left). For each stage, the temporal distribution of microseismic events during injection is shown by the grey histogram. Cumulative area is indicated on the same axes by the black line.

The correlation between production and cumulative microseismic source area is significantly stronger than the correlation between production and the number of detected events. Note that stage 2 has more microearthquakes than stages 4 or 6, but much less area was created and there was much less production. As Figure 6 does not take into account the location of the events, the average magnitude of events during stage 2 must be smaller than that of stages 4 and 6. It is also important to note the area created during stimulation of a given stage may not occur in the same place as the stage and thus not contribute to the stage's production. As noted above, zonal isolation seems to affect stage 2 events, and Farghal and Zoback (2015) noted that some of the events associated with stage 2 appear to have been channelized along a NE-SW trending pre-existing fault damage zone (note the events near monitoring well A). Thus, while the number of events created during stage 2 might have led one to expect higher production than what was

observed, both the small size of the events and their scattered locations resulted in relatively little production.

Another way to evaluate the relationship between the stimulated fracture network and production is to quantify the distribution of diffusion distances between the low permeability matrix (where the hydrocarbons reside) and high permeability fractures within the stimulated volume. These distances can then be used to approximate the percentage of the target volume drained as a function of time. Another way to think about this is that because the rock is so impermeable, hydrocarbons can only flow a limited distance in a given amount of time. On time scales relevant to production (several years), stimulated faults and fractures in low permeability reservoirs can generally be considered to have infinite effective permeability relative to the matrix. Thus, production rates are limited by the rate of diffusion from the matrix to the high permeability network (Walton and McLennan, 2013). Thus, it is not only important to create surface area during stimulation, it is important to create this area distributed throughout the target reservoir volume in order to have permeable fracture planes relatively close to the majority of hydrocarbon-bearing pores in the matrix.

Linear flow is characterized by flow from the matrix to a highly permeable plane in the direction normal to that plane, whether it is the hydraulic fracture or a stimulated shear fracture. The high permeability of the planes is such that pressure in the plane can be considered constant. In the context of linear flow, particle transport can be modeled by a 1-D diffusive process, for which the characteristic diffusion time, τ, is given by Eq. 5,

$$\tau = \frac{l^2}{\kappa} = \frac{(\phi B_f + B_r)\eta l^2}{k} \quad (6)$$

where l is the characteristic diffusion distance, $\kappa \approx \frac{k}{\eta(\phi B_f + B_r)}$ is the hydraulic diffusivity, B_f and B_r are fluid and rock compressibilities, ϕ is rock porosity, and η is fluid viscosity. Using mechanical properties of Barnett I cores and the geomechanical setting, the characteristic diffusion times can be constructed for various permeabilities using $B_f = 3 * 10^{-8}\ Pa^{-1}$, $B_r = 6 * 10^{-11}\ Pa^{-1}$, $\phi = 0.1$, and $\eta = 3.5 * 10^{-5} Pa\ \cdot s$.

The resulting relationship for natural gas and oil in linear and log space is shown black and red, respectively, in Figure 7. The 3-year characteristic diffusion distance for gas in a 100 nanodarcy reservoir is approximately 10 meters. Fundamentally, this means that in three years, gas can flow only about 10 meters from a matrix pore to a permeable fracture. Hence, if a sufficiently dense network of fractures is not formed by stimulation, there will not be sufficient production in three years to justify the cost of development. Because of its higher viscosity, the situation is much worse for oil. For a matrix permeability of 100 nanodarcies, the diffusion distance is only about 2.5 meters.

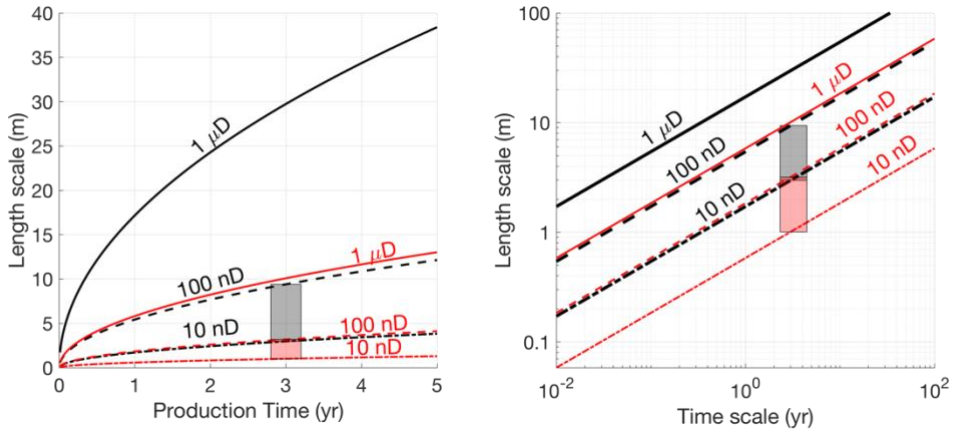

Figure 7: The time required for methane to diffuse through typical matrix permeabilities is given on a liner scale on the left and log-log scale on the right. The grey region indicates that approximately three years are required for gas to diffuse approximately 3-10 meters through 10-100 nanodarcy matrix to a high permeability pathway. The corresponding time/distance relationship for oil is shown in red, with an approximately factor of 10 higher viscosity resulting in a corresponding decrease in diffusion distances. The gray and pink boxes reflect a representative range of matrix permeabilities for unconventional reservoirs (e.g., Heller et al., 2014).

This analysis provides insight into the importance of low viscosity frac fluids and leak off during the stimulation process. For example, if there are 8 rectangular hydraulic fractures (one from each perforation cluster, 50 meters apart) created during each stage in the Barnett II case study with a propped length of 200 meters and a propped a height of 50 meters, the total permeable surface are of the hydraulic fractures would be 80,000 m^2, comparable to the lower bound estimate of the surface area of the stimulated fracture network. However, the diffusion distance between hydrofracs 50 meters apart would make the diffusion times for flow far too long to be economically practical. Said another way, while large hydraulic fractures could create sufficient area to produce hydrocarbons, it would only be economically practical if the hydraulic fractures were spaced about 10 meters apart.

Ideally, the stimulated fracture network is relatively homogenously distributed in the target volume, resulting in relatively short diffusion distances to the nearest fracture. Figure 8 attempts to combine the concepts of area and diffusion time by characterizing the efficacy of each stage in terms of distribution diffusion times to the high permeability fracture network in a

volume with an average matrix permeability of 100 nD. The percentage of the theoretical stimulated reservoir volume of each stage (on the y-axis) within a mean diffusion time (on the x-axis) is displayed as a function of time during stimulation (color contours). The target reservoir volume is fixed for each stage. The dimensions are given by the well spacing, stage spacing, and thickness of the target formation, with the center of the perforation cluster at the center of the volume. Following generation of the fracture network from microseismicity, a distribution of distances to the nearest stimulated fracture is calculated. Converting from distance to mean diffusion time then provides insight into production over time. This method excludes area created outside the target zone. For example, much of the area created by stage 2 was outside the target zone, resulting in only 22% of the target reservoir volume being in the 3-year diffusion window. Note that the strong majority of the target volume ultimately brought within 3 years of diffusion time to the permeable network is accessed in the first 90 minutes of pumping. Stage 7 is the only exception, with target volume penetration roughly doubling between 90 and 180 minutes of pumping. In other words, this analysis suggests that far more fluid than necessary was pumped in 7 of the 8 stages.

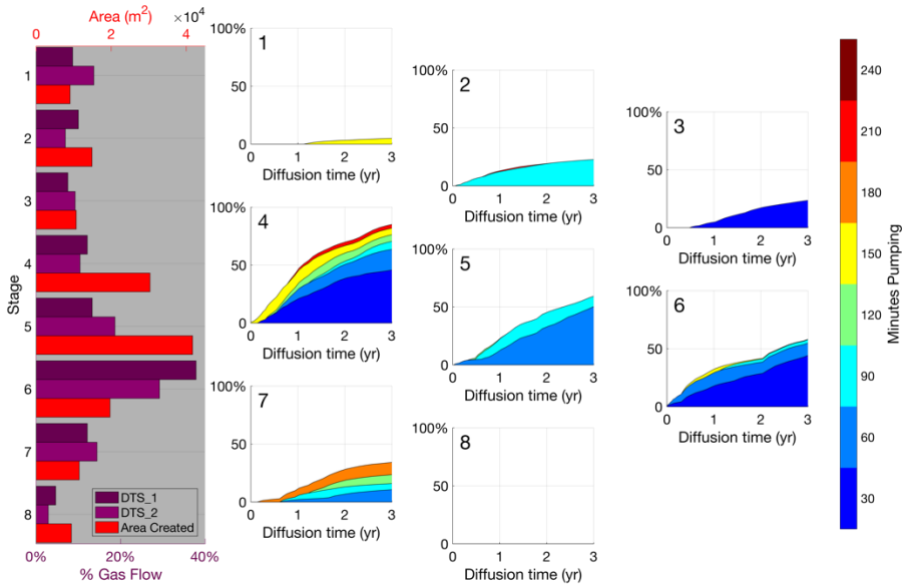

Figure 8: The distribution of distances to the nearest high permeability pathways is key to understanding production. By modeling the fracture network and calculating the distribution of distances to permeable zones across the reservoir volume, an estimate of the drained portion of the target volume is calculated as a function of time assuming an average matrix permeability of 100 nD.

Conclusions

The production decline rates in four unconventional gas and oil reservoirs in the continental United States indicate that linear flow dominates the economically crucial early years of production. The good fit of the production rates from the four reservoirs considered indicates that the rapid decrease in production rates is a natural consequence of depletion in these extremely low permeability formations. In this flow regime, production increases linearly with permeable surface area created through shearing of pre-existing fractures and faults during slick-water frac'ing. Accordingly, to maximize production, hydraulic fracturing stimulation should attempt to maximize area creation in a relatively well-distributed fracture network. We demonstrated that one can assess the evolution of cumulative surface area as injection proceeds. For the simple, first-order analysis presented here, neither precise event locations nor focal plane mechanisms are required.

REFERENCES

Al-Ismail, MI, and MD Zoback. 2016. "Effects of Rock Mineralogy and Pore Structure on Extremely Low Stress-Dependent Matrix Permeability of Unconventional Shale Gas and Shale Oil Samples." *Royal Society Philosophical Transactions A*. doi:10.1098/rsta.2015.0428.

Allmann, BP, and PM Shearer. 2009. "Global Variations of Stress Drop for Moderate to Large Earthquakes." *Journal of Geophysical Research: Solid Earth* 114 (1): 1–22. doi:10.1029/2008JB005821.

Bhandari, AR, PB Flemings, PJ Polito, MB Cronin, and SL Bryant. 2015. "Anisotropy and Stress Dependence of Permeability in the Barnett Shale." *Transport in Porous Media* 108 (2). Springer Netherlands: 393–411. doi:10.1007/s11242-015-0482-0.

Clerc, F, RM Harrington, Y Liu, and YJ Gu. 2016. "Stress Drop Estimates and Hypocenter Relocations of Induced Seismicity near Crooked Lake, Alberta." *Geophysical Research Letters* 43 (13): 6942–51. doi:10.1002/2016GL069800.

Cocco, M, E Tinti, and A Cirella. 2016. "On the Scale Dependence of Earthquake Stress Drop." *Journal of Seismology* 20 (4). Journal of Seismology: 1151–70. doi:10.1007/s10950-016-9594-4.

Farghal, NS, and MD Zoback. 2015. "Identification of Slowly Slipping Faults in the Barnett Shale Utilizing Ant Tracking; Identification of Slowly Slipping Faults in the Barnett Shale Utilizing Ant Tracking," 4919–23. doi:10.1190/segam2015-5811224.1.

Gale, JFW, SE Laubach, JE Olson, P Eichhuble, and A Fall. 2014. "Natural Fractures in Shale:

A Review and New Observations." *AAPG Bulletin* 98 (11): 2165–2216. doi:10.1306/08121413151.

Goertz-Allmann, BP, A Goertz, and S Wiemer. 2011. "Stress Drop Variations of Induced Earthquakes at the Basel Geothermal Site." *Geophysical Research Letters* 38 (9): 1–5. doi:10.1029/2011GL047498.

Hakso, A, and M Zoback. 2017. "Utilizing Multiplets as an Independent Assessment of Relative Microseismic Location Uncertainty." *The Leading Edge* 36 (10): 829–36. doi:10.1190/tle36100829.1.

Heller, R, J Vermylen, and M Zoback. 2014. "Experimental Investigation of Matrix Permeability of Gas Shales." *AAPG Bulletin* 98 (5): 975–95. doi:10.1306/09231313023.

Huang, Y, GC Beroza, and WL Ellsworth. 2016. "Stress Drop Estimates of Potentially Induced Earthquakes in the Guy-Greenbrier Sequence." *Journal of Geophysical Research: Solid Earth* 121 (9): 6597–6607. doi:10.1002/2016JB013067.

Imanishi, K, and WL Ellsworth. 2006. "Source Scaling Relationships of Microearthquakes at Parkfield, CA, Determined Using the SAFOD Pilot Hole Seismic Array." In *Earthquakes: Radiated Energy and the Physics of Faulting*, 81–90. American Geophysical Union. doi:10.1029/170GM10.

Katz, DLV. 1959. *Handbook of Natural Gas Engineering*. McGraw-Hill.

Kohli, AH, and MD Zoback. 2013. "Frictional Properties of Shale Reservoir Rocks." *Journal of Geophysical Research: Solid Earth* 118 (April): 5109–25. doi:10.1002/jgrb.50346.

Kuang, W, M Zoback, and J Zhang. 2017. "Estimating Geomechanical Parameters from Microseismic Plane Focal Mechanisms Recorded during Multistage Hydraulic Fracturing."

Geophysics 82 (1): KS1-KS11. doi:10.1190/geo2015-0691.1.

Luffel, DL, CW Hopkins, and PD Schettler. 1993. "Matrix Permeability Measurement of Gas Productive Shales." In *Proceedings of SPE Annual Technical Conference and Exhibition*, 261–71. doi:10.2523/26633-MS.

Maxwell, SC. 2014. *Microseismic Imaging of Hydraulic Fracturing : Improved Engineering of Unconventional Shale Reservoirs*. *Society of Exploration Geophysicists*. doi:10.1190/1.9781560803164.

Patzek, T, F Male, and M Marder. 2014. "A Simple Model of Gas Production from Hydrofractured Horizontal Wells in Shales." *AAPG Bulletin* 98 (12): 2507–29. doi:10.1306/03241412125.

Roy, B, B Hart, A Mironova, C Zhou, and U Zimmer. 2014. "Integrated Characterization of Hydraulic Fracture Treatments in the Barnett Shale: The Stocker Geophysical Experiment." *Interpretation* 2 (2): T111–27. doi:10.1190/INT-2013-0071.1.

Stein, S, and M Wysession. 2003. *An Introduction to Seismology, Earthquakes, and Earth Structure*. John Wiley & Sons. doi:10.1785/gssrl.74.6.824.

Walton, I, and J McLennan. 2013. "The Role of Natural Fractures in Shale Gas Production." *Effective and Sustainable Hydraulic Fracturing*. doi:10.5772/56404.

Ye, Z, M Janis, A Ghassemi, and S Riley. 2017. "Laboratory Investigation of Fluid Flow and Permeability Evolution through Shale Fractures," 24–26. doi:10.15530/urtec-2017-2674846.

Zoback, MD, A Kohli, I Das, and M Mcclure. 2012. "The Importance of Slow Slip on Faults During Hydraulic Fracturing Stimulation of Shale Gas Reservoirs." In *Americas*

Unconventional Resources Conference. doi:10.2118/155476-MS.